Materials Characterization 215 (2024) 114120

Contents lists available at ScienceDirect

Materials Characterization

journal homepage: www.elsevier.com/locate/matchar

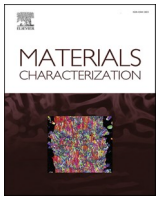

Effects of Y_2O_3 on the hot deformation behavior and microstructure evolution of Al_2O_3-cu/35Cr3TiB_2 electrical contact composites

Zipeng Ma [a], Meng Zhou [a,**], Heng Li [a], Ke Jing [a], Jiacan Zhang [a], Baohong Tian [a,b,*], Yi Zhang [a,b,*], Xu Li [c], Haoyan Hu [a], Alex A. Volinsky [d]

[a] School of Materials Science and Engineering, Henan University of Science and Technology, Provincial and Ministerial Co-Construction of Collaborative Innovation Center for Non-ferrous Metals New Materials and Advanced Processing Technology, Luoyang 471023, PR China
[b] Henan Province Key Laboratory of Nonferrous Materials Science and Processing Technology, Luoyang 471023, PR China
[c] Center for Advanced Measurement Science, National Institute of Metrology, Beijing 100029, PR China
[d] Department of Mechanical Engineering, University of South Florida, 4202 E. Fowler Ave. ENG 030, Tampa 33620, USA

ARTICLE INFO

Keywords:
Copper-based composites
Hot deformation behavior
Dynamic recrystallization
Microstructure evolution

ABSTRACT

The Al_2O_3-Cu/35Cr3TiB_2 and $0.5Y_2O_3/Al_2O_3$-Cu/35Cr3TiB_2 composites were prepared by a combination of fast hot compression sintering and internal oxidization. The effects of Y_2O_3 on the hot deformation behavior and microstructure evolution of the composites were investigated. According to the hot deformation data, the constitutive equations, hot processing maps, and critical dynamic recrystallization models were constructed for the two composites. The Y_2O_3 addition enhanced the flow stress, activation energy, and hot processing properties of the composites. This led to a reduction in the percentage of dynamic recrystallization structure from 25.3% to 19.4%, and decreased the amount of high-angle grain boundaries from 77.8% to 71.4%. Y_2O_3 was distributed at grain boundaries and phase interfaces, effectively impeding dislocation movement and grain boundary migration. Notably, the strain distribution within Y_2O_3 exhibited greater homogeneity compared to the Cu matrix. More twins and stacking faults were observed inside the $0.5Y_2O_3/Al_2O_3$-Cu/35Cr3TiB_2 composites, which synergistically strengthened the matrix.

1. Introduction

Copper is widely used in various fields such as electrical engineering, automotive industry and high voltage contacts due to its high electrical and thermal conductivity, along with other physical properties [1–3]. Electrical contacts are some of the core components of all kinds of high-end instruments and switchgear, and are of great significance in improving the core competitiveness of the equipment manufacturing industry [4,5]. With the rapid development of modern industry, all kinds of instruments are pursuing lightweight and functional diversification, which put forward higher requirements for the performance of electrical contact materials [6]. However, due to the low melting point, copper and copper alloys melt and weld together under the influence of arc heat and other factors when used as contacts, severely limiting their service life and the application of copper in the field of electrical contacts [7,8].

Adding high-strength and high-hardness secondary phases to the copper matrix can effectively improve the material's properties and achieve a combination of good performance with little impact on the original properties of copper [9,10]. By regulating the type, quantity and distribution of the reinforcing phases in the matrix, and even the way the reinforcing phases are combined with the copper matrix, composites with different properties can be developed and applied in different fields [11]. Therefore, copper-based composites are widely used as electrical contacts, especially Cu—Cr contacts with good breaking capacity and arc erosion resistance [12,13]. Although the fabrication principles of Cu-matrix composites ensure the diversity of their properties and applications, their manufacturing is more complicated than traditional alloys. The most commonly used fabrication method is the powder metallurgy [14,15], but it is limited to small product size, long process cycle and high production cost, making it impractical for mass production. Secondary processing of the formed material is often required from production to application. Compared with copper alloys, copper matrix

* Corresponding authors at: School of Materials Science and Engineering, Henan University of Science and Technology, Provincial and Ministerial Co-Construction of Collaborative Innovation Center for Non-ferrous Metals New Materials and Advanced Processing Technology, Luoyang 471023, PR China.
** Corresponding author.
E-mail addresses: zhoumeng0902@126.com (M. Zhou), bhtian007@163.com (B. Tian), zhshgu436@163.com (Y. Zhang).

https://doi.org/10.1016/j.matchar.2024.114120
Received 22 March 2024; Received in revised form 31 May 2024; Accepted 25 June 2024
Available online 26 June 2024

composites have poor processing performance and are prone to macroscopic cracks during processing resulting in raw material loss. While many researchers have focused on the arc erosion resistance of electrical contact materials, limited research has been done on the hot processing performance of materials. Only the electrical contact materials with both hot processing performance and electrical contact performance can comply with the future developments of large-scale manufacturing for a wide range of applications.

Hot deformation is an important part of hot processing, and the relationship between deformation temperature, strain rate and microstructure evolution during hot deformation is important for the process optimization [16,17]. Excellent hot processing can improve the microstructure of the composites and refine the grains, thus enhancing the comprehensive performance of the materials [18,19]. Many researchers have studied the hot deformation behavior and microstructure evolution of composites in recent years [20–22]. Feng et al. [23] comprehensively analyzed the microstructure, mechanical properties and electrical conductivity of Cu-0.4 wt% Al_2O_3 composite, and found that the composite possessed a tensile strength of 560 MPa and an electrical conductivity of 87.5% IACS after cold-drawing, and a microhardness of 125 HV after annealing at 900 °C, implying that the Cu-0.4 wt% Al_2O_3 composite possessed good thermal stability. Ban et al. [24] investigated the effects of Cr addition on the hot deformation behavior of copper alloys and found that Cr improves the structural properties, reduces the size of the precipitated phases and increases their number, thus increasing the activation energy of the alloy. Xiao et al. [25] found that the TiB_2 particles significantly increased the activation energy of the composites, hindering the migration of grain boundaries, and leading to finer dynamic recrystallization (DRX) grains. Chen et al. [26] investigated the effects of TiB_2 on the hot processing properties of aluminum matrix composites and reported that the peak stress increased with more TiB_2, gradually changing the softening mechanism from DRX + dynamic recovery to just dynamic recovery. The application of rare earth elements in the hot deformation of materials has also received considerable attention. Xu et al. [27] found that the addition of Y reduced the unstable processing region of copper alloys during hot deformation and promoted DRX. Ahamed et al. [28] prepared Al6063/0.75Al_2O_3/0.75Y_2O_3 composites and found that the higher activation energy of the nanocomposites was attributed to the action of nano-Al_2O_3 and nano-Y_2O_3 hard ceramic particles, which fixed the movement of dislocations and grain boundaries during hot deformation and improved the deformation resistance. Based on these studies, the addition of the hard phases increases the activation energy of the materials, but there are no definitive conclusions of the Y_2O_3 effects on the machinability and structure evolution during hot deformation of the materials.

Previous studies have shown that Al_2O_3-Cu/35Cr3TiB_2 composites have good electrical contact properties, and the addition of Y_2O_3 enhances electrical contact properties, improving application prospects [29]. The hot deformation behavior of Al_2O_3-Cu/35Cr3TiB_2 composites was investigated in this study, and the effects the of Y_2O_3 addition on the recrystallization behavior and the structure evolution of the composites during hot deformation were analyzed. By constructing the hot processing maps of the two composites and analyzing their hot processing stability, the optimal processing temperature and strain rate of the composites can be determined. It is conducive to the refinement of molding and reduction of material loss in production, and provides a theoretical basis for the subsequent processing technology and practical applications of the materials.

2. Experiments

2.1. Composites fabrication

In preparing the two composites, the average particle size of 37 μm Cu-0.4Al (Al 0.4 wt%) alloy powder, 2–5 μm Cu_2O powder, average particle size of 37 μm Cr powder, 3–5 μm TiB_2 powder and average particle size of 50 nm Y_2O_3 powder were placed into a plastic ball milling jar according to the proportions shown in Fig. 1. Pure copper balls with 3 mm and 5 mm diameters were added at a ball-to-materials ratio of 5:1 and stirred at 50 rpm for 6 h in a QQM/B ball mill. The mixed powder was then placed into a graphite mold, and graphite paper was used to separate the powder from the mold to prevent the powder from sticking to the mold. This can effectively reduce demolding and improve the service life of the mold. Subsequently, the powder in the mold was subjected to cold isostatic pressing to compress the powders and make them denser. This also reduces oxidation during sintering, and improves the heat transfer efficiency of the powders, thus reducing the time for the overall heating and forming of the powders. Finally, the graphite mold was placed into the FHP-828 fast hot press sintering furnace, vacuumed below 1 Pa, and then the program was initiated to start the temperature rise at 100 °C/min heating rate and longitudinal compression of the mold. After 8 min, the temperature and pressure reached the set values of 800 °C and 40 MPa and were held for 2 min, after which the temperature and pressure were increased to reach the final 950 °C temperature and 45 MPa pressure, and the mold was held in this state for 15 min. It is worth noting that the pressure is not unloaded directly during the cooling down process after the sintering is completed, but when the temperature drops to 500 °C, the pressure is unloaded, which can make the structure of the composites denser. When the furnace temperature drops to room temperature the mold is removed and demolded, and two composites are successfully prepared.

2.2. Hot deformation testing

The sintered samples were cut into several Φ8 mm × 12 mm cylinders and tested in compression using a Gleeble-1500D testing machine at 650 °C, 750 °C, 850 °C, and 950 °C temperatures and 1 s^{-1}, 0.1 s^{-1}, 0.01 s^{-1}, and 0.001 s^{-1} strain rates. The process flow is shown in Fig. 2 (a), in the hot deformation test, the samples are heated to the specified temperature with the furnace, and the heating rate is 10 °C/s. After reaching the specified temperature, the samples are held for 3 min, so that the composites as a whole are heated uniformly to ensure the rigor of the test. Subsequently, the composites were compressed, and water quenching and fast cooling were performed immediately after the completion of compression to preserve the structure of the materials during deformation at elevated temperatures for subsequent observation and analysis.

2.3. Microstructure characterization

As shown in Fig. 2(b), a slice was cut out from compressed samples in the middle and polished to observe the changes of the internal structure after hot compression. Subsequently, the sheet samples were subjected to ion-thinning treatment and their microstructure was characterized using a LIBRA-200FE transmission electron microscope, followed by electron backscattering diffraction (EBSD) characterization of the composites in the sintered state and after hot compression using a JSM-7800F scanning electron microscope.

3. Results

3.1. True stress-true strain curves

The flow stress is an important engineering parameter that characterizes the deformation properties of the materials during the hot deformation process, and determines the degree of force and the amount of energy required in the deformation process. Fig. 3 shows the true stress-true strain curves of the two composites deformed under different temperatures and strain rates. All curves show DRX characteristics where the stress will rise sharply at the beginning of the deformation, slowly increasing to the peak stress, and then reducing at higher strain. This is because, on the one hand as the isothermal compression test

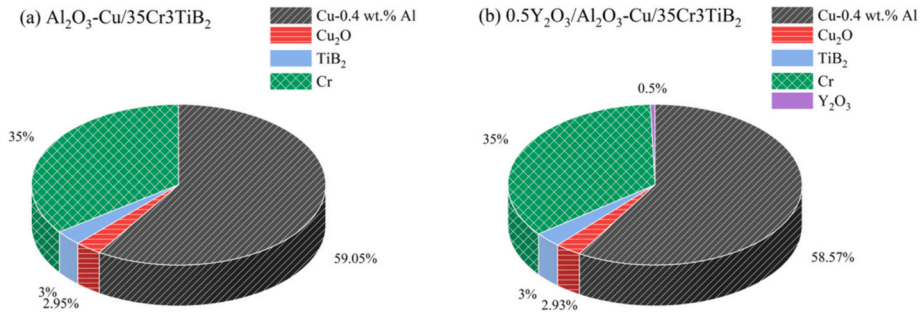

Fig. 1. Ratio of raw materials for composites: (a) Al_2O_3-Cu/35Cr3TiB_2 and (b) 0.5Y_2O_3/Al_2O_3-Cu/35Cr3TiB_2.

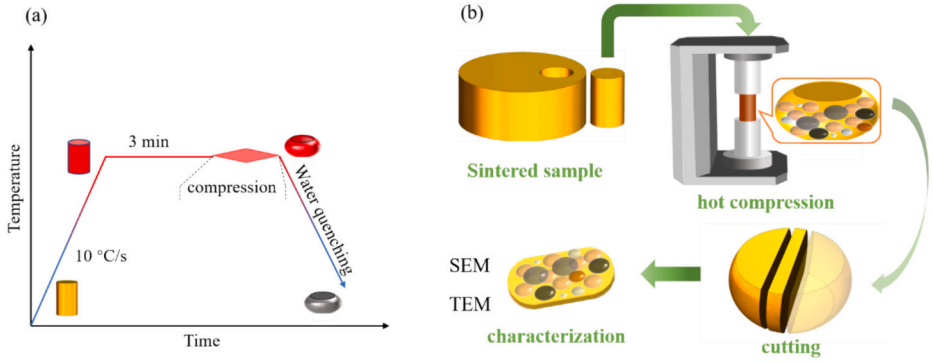

Fig. 2. Hot deformation experiments: (a) temperature profile, (b) experimental process flow.

progresses, the dislocation density inside the composites gradually increases, and the dislocations become entangled or defects such as dislocation cells are formed, which impede the dislocations from moving further, so that the force required to continue the deformation of the composites increases rapidly [24]. On the other hand, by increasing degree of matrix deformation and the multiplication of dislocations, caused by the lattice distortion, stress field and other defects, the deformation stored energy will be converted into a dynamic recovery and DRX driving force [20,27]. When accumulated to a certain extent, the material undergoes dynamic recovery and DRX and thus softens, so that the force required to continue the deformation of the material is reduced [30]. This is a dynamic process in which the dominant party ultimately determines the rise and fall of stress.

For a given temperature, the peak stress decreases gradually as the strain rate decreases from 1 s^{-1} to 0.001 s^{-1}. A lower strain rate means that the longer it takes to compress to a certain strain, the more time there is for dynamic recovery and DRX to occur within the material, which start to dominate earlier, allowing peak stresses to occur faster, leading to an overall reduction of the flow stresses in the material. For the same strain rate, the flow stress of the material shows a decreasing trend as the temperature increases, while the stress peak appears earlier. This is because the increase in temperature leads to a decrease in the bonding energy between the atoms and the bonds are more easily broken. And the increase in temperature is conducive to the movement and diffusion of atoms inside the composite material, the slip and climb of dislocations and the transfer of vacancies are easier, and the material will undergo DRX and grains growth process more quickly. On the other hand, the increase in temperature contributes to the growth of grains, and the growth of DRX grains also reduces the deformation resistance of the material.

It can be seen from Fig. 3 that the flow stress of the composites increased significantly after the addition of Y_2O_3, which is likely due to the fact that the hard Y_2O_3 phase uniformly distributed in the matrix impedes the movement of dislocations and grain boundaries, and increased the resistance to further deformation of the materials. On the other hand, at higher temperatures, compared to the Al_2O_3-Cu/35Cr3TiB_2 composites, the addition of Y_2O_3 reduces the magnitude of the composites' flow stress decrease after it reaches the peak value, which leads to an increase in the slope of the curves under the stress reduction stage. This means that the Y_2O_3 addition inhibits the softening of the composites under the same deformation conditions. When the deformation degree is large, the dislocations within the material rapidly increase in value, resulting in dislocation cells formed by dislocation tangles. During the heating process, the walls of the dislocation cells are flattened to form subcrystals, which are then used as the core for DRX to produce distortion-free equiaxed grains. Whereas the softening effect of DRX on the material is more pronounced compared to the dynamic recovery, so the addition of Y_2O_3 inhibits the DRX of the composites.

3.2. Constitutive equations

The flow stress depends on the deformation temperature and strain rate of the hot deformation tests. Constitutive equations describe the mathematical relationship between deformation temperature, strain rate and flow stress of the materials during hot processing, which is of great significance for the process design and practical applications. It can reflect the nature and behavior of the materials, which is of guiding significance for the prediction and optimization of materials properties, etc., and provides theoretical support for the subsequent processing and precision molding of composites. The commonly used models for the constitutive equations are power, exponential and hyperbolic sine [31–33]:

$$\dot{\varepsilon} = A_1 \sigma^{n_1} exp\left(-\frac{Q}{RT}\right) \quad \alpha\sigma < 0.8 \tag{1}$$

$$\dot{\varepsilon} = A_2 exp\left(\beta\sigma - \frac{Q}{RT}\right) \quad \alpha\sigma > 1.2 \tag{2}$$

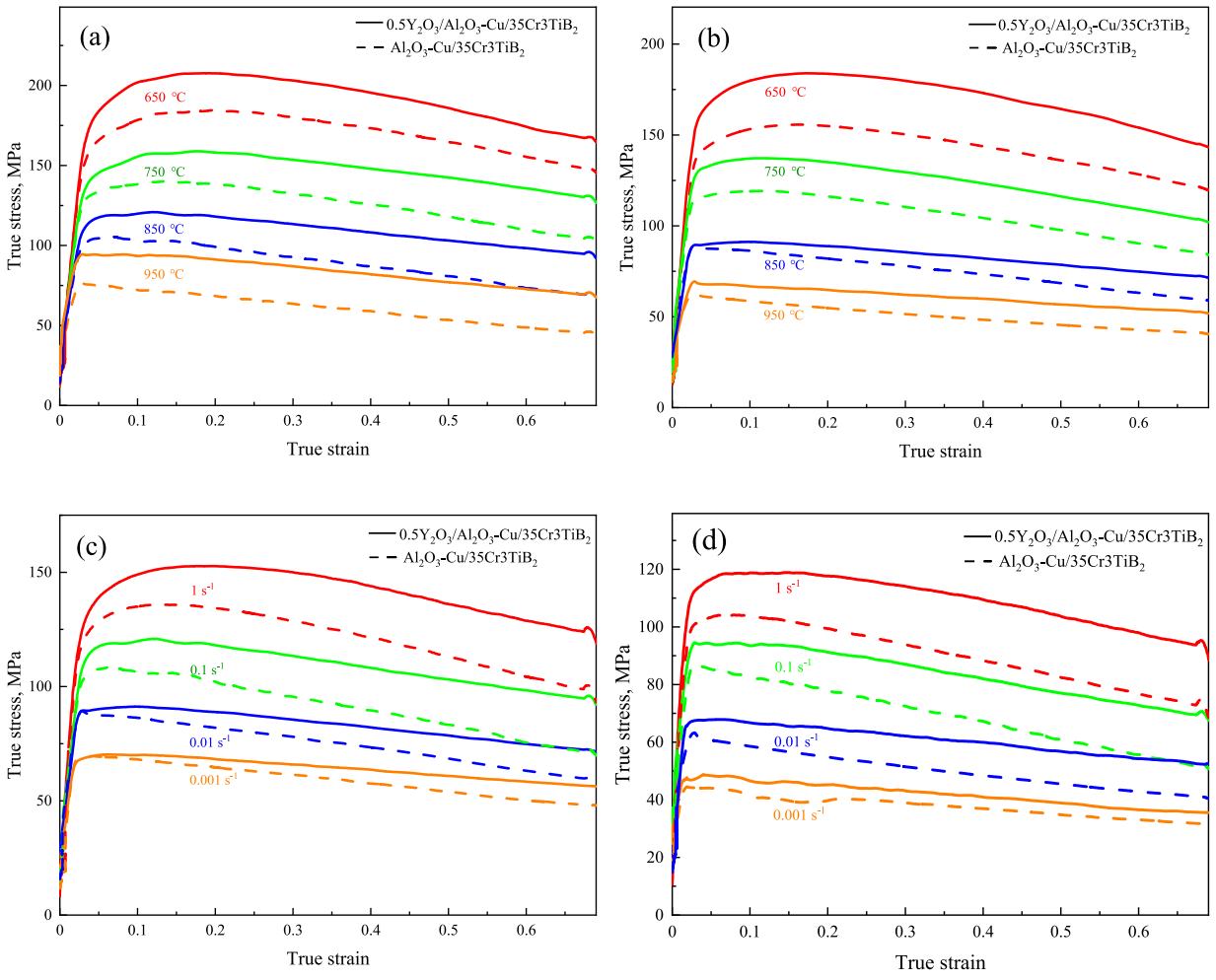

Fig. 3. True stress-true strain curves of the Al_2O_3-Cu/35Cr3TiB_2 and 0.5Y_2O_3/Al_2O_3-Cu/35Cr3TiB_2 composites under different deformation conditions: (a) 0.1 s^{-1}, (b) 0.01 s^{-1}, (c) 850 °C, (d) 950 °C.

$$\dot{\varepsilon} = \mathrm{A}[sinh\,(\alpha\sigma)]^{\mathrm{n}} exp\left(-\frac{Q}{\mathrm{RT}}\right) \text{ (For all)} \tag{3}$$

Here, $\dot{\varepsilon}$ represents the strain rate (s^{-1}), σ is the maximum stress (MPa), T is the test temperature (K), R is the molar gas constant (8.314 J/mol·K), Q is the material activation energy (kJ/mol), and the rest are material's correlation coefficients. Taking logarithms of Eqs. (1)–(3) yields:

$$ln\,\dot{\varepsilon} = \mathrm{n}_1 ln\,\sigma + ln\,\mathrm{A}_1 - \frac{Q}{\mathrm{RT}} \tag{4}$$

$$ln\,\dot{\varepsilon} = \beta\sigma + ln\,\mathrm{A}_2 - \frac{Q}{\mathrm{RT}} \tag{5}$$

$$ln\,\dot{\varepsilon} = \mathrm{n}\,ln[sinh\,(\alpha\sigma)] + ln\,\mathrm{A} - \frac{Q}{\mathrm{RT}} \tag{6}$$

Among the three models of the constitutive equations, the power law equation is only applicable to low stress levels (ασ < 0.8), the exponential equation is applicable to high stress levels (ασ > 1.2), and the hyperbolic sine function model is applicable to all stress conditions. In order to compare constitutive equations of different materials under different stress levels in the subsequent work, the hyperbolic sine function model with the widest applicability was chosen for both composites.

Based on Eq. (3):

$$\mathrm{Q} = \mathrm{R}\left[\frac{\partial(ln\dot{\varepsilon})}{\partial ln[sin(\alpha\sigma)]}\right]_{\mathrm{T}}\left[\frac{\partial ln[sinh(\alpha\sigma)]}{\partial(1/T)}\right]_{\dot{\varepsilon}} = \mathrm{RnS} \tag{7}$$

The Zener-Hollomon parameter Z denotes the combined effects of strain rate and deformation temperature on the flow stress:

$$\mathrm{Z} = \dot{\varepsilon}\, exp\left[\frac{Q}{RT}\right] \tag{8}$$

This can be obtained by substituting Eq. (8) into Eq. (3):

$$ln\,\mathrm{Z} = ln\,A + n\,ln\,[sinh(\alpha\sigma)] \tag{9}$$

The peak stresses of the true stress-true strain curves of Al_2O_3-Cu/35Cr3TiB_2 composites under different deformation conditions were calculated by substituting them into Eq. (3), and the relationship curves between strain rate, deformation temperature, and flow stress were obtained in Fig. 4. It can be seen based on the relationship between the different parameters in each equation that n_1, β, n, and S correspond to the average slopes of the lines in Fig. 4(a-d), respectively. Then n_1 = 11.556, β = 0.095, α = β/n_1 = 0.008, n = 8.274, and S = 4.498. When the value of ln[sinh(ασ)] is 0 in Eq. (9), the values of lnZ and lnA are equal. Therefore, plotting ln[sinh(ασ)] and lnZ as horizontal and vertical coordinates, and fitting, one gets lnA = 31.168. Substituting the corresponding values into Eq. (7) yields the activation energy of the material as 309.418 kJ/mol. Similarly, the activation energy of the 0.5Y_2O_3/Al_2O_3-Cu/35Cr3TiB_2 composites is 341.541 kJ/mol, and the addition of Y_2O_3 increases the activation energy of the composites by 10.4%, which

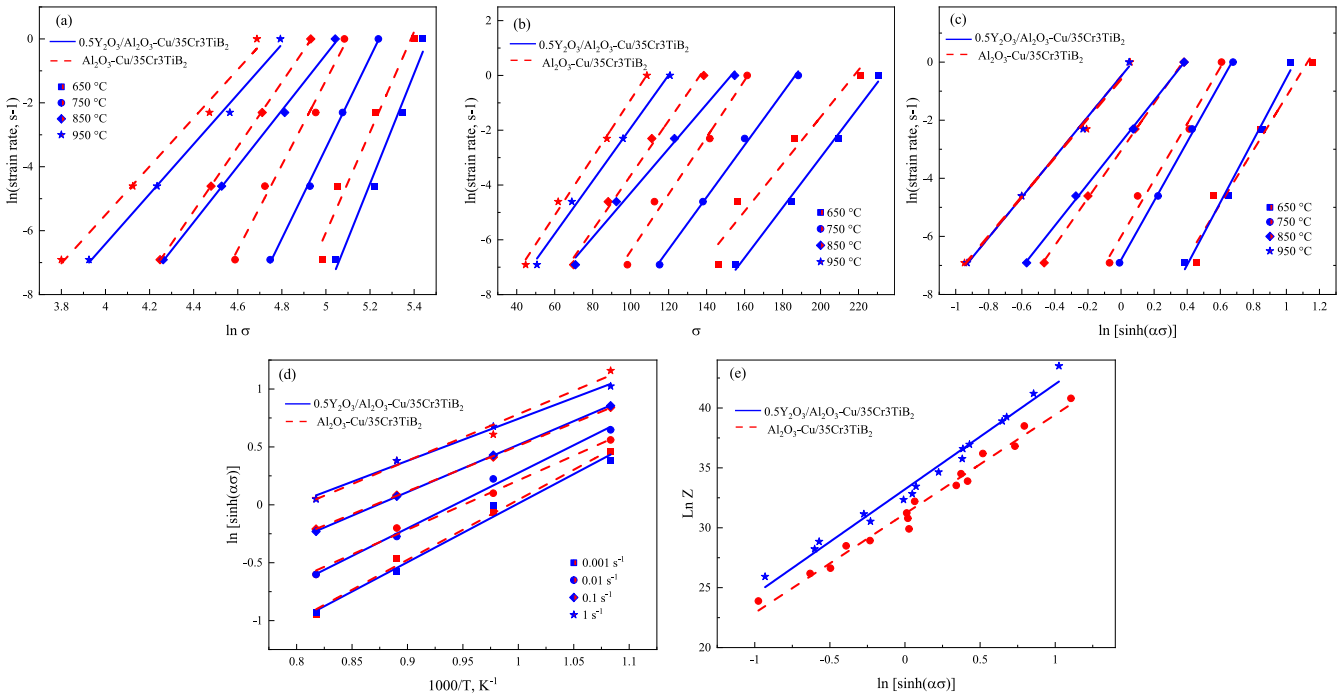

Fig. 4. Functional relationships between deformation rate, peak stress and deformation temperature of the two composites: (a) ln$\dot{\varepsilon}$-lnσ; (b) ln$\dot{\varepsilon}$-σ; (c) ln$\dot{\varepsilon}$-ln [sinh (ασ)]; (d) ln[sinh(ασ)]-1/T; (e) lnZ-ln [sinh(ασ)].

implies an improvement in the deformation resistance of the composites. Then the constitutive equations of the Al_2O_3-Cu/35Cr3TiB_2 and 0.5Y_2O_3/ Al_2O_3-Cu/35Cr3TiB_2 composites are, respectively:

$$\dot{\varepsilon} = [sinh 0.008\sigma]^{8.274} exp\left(31.168 - \frac{309418}{8.314T}\right) \tag{10}$$

$$\dot{\varepsilon} = [sinh 0.008\sigma]^{8.948} exp\left(33.218 - \frac{341541}{8.314T}\right) \tag{11}$$

3.3. Critical DRX model

It can be seen from the above analysis that the material will undergo DRX during hot deformation, but it is not possible to specify under what stage the material starts to undergo DRX. The effects of temperature and strain rate on the critical point of DRX occurrence are not clear, which is not conducive to the analysis of the material's processing properties and structure evolution. Poliak et al. [34] showed that the strain corresponding to the location of the inflection point in the curve of the relationship between the work-hardening curvature θ (θ = $\partial\sigma/\partial\varepsilon$) and the stress σ of the material is the DRX critical strain. Based on this, lnθ-ε and -$\partial(\ln\theta)/\partial\varepsilon$-ε curves can be plotted according to the true stress-true strain curves of the material, then when the value of -$\partial^2(\ln\theta)/\partial\varepsilon$ is 0, the corresponding strain value is the critical DRX strain value of the material under the same deformation conditions.

Since the true stress-true strain curves obtained from the hot deformation tests were not completely smooth, they were fitted according to Eq. (12), and the correlation coefficients R^2 after fitting were all >0.99:

$$\sigma = \frac{a + b\varepsilon + c\varepsilon 2 + d\varepsilon 3 + e\varepsilon 4 + f\varepsilon 5 + g\varepsilon 6}{h + i\varepsilon + j\varepsilon 2 + k\varepsilon 3 + l\varepsilon 4 + m\varepsilon 5 + n\varepsilon 6 + o\varepsilon 7} \tag{12}$$

$$ln\theta = A - B\varepsilon + C\varepsilon 2 - D\varepsilon 3 \tag{13}$$

The a-o in Eq. (12) are constants, and the fitted curves for the Al_2O_3-Cu/35Cr3TiB_2 composites deformed at 850 °C and 0.01 s^{-1} are shown in Fig. 5(a). Differentiating the fitted equation gives the work-hardening rate θ, which is the rate at which the degree of hardening of the material changes with the strain during plastic deformation. Plotting the lnθ-ε curve and fitting Eq. (13) provides the specific location of the inflection point in Fig. 5(b). Then the derivation is performed again to obtain the -$\partial(\ln\theta)/\partial\varepsilon$-ε relationship curve in Fig. 5(c). The point where the slope of the curve is 0 corresponds to the inflection point of the lnθ-ε curve, so the strain value 0.272 corresponding to the lowest point of the $\partial(\ln\theta)/\partial\varepsilon$-ε curve is the critical strain for DRX of the Al_2O_3-Cu/35Cr3TiB_2 composites under this deformation condition.

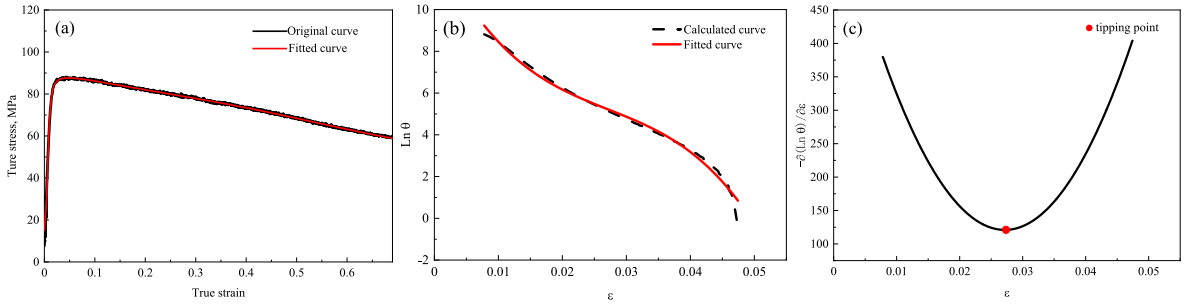

Fig. 5. True stress-true strain curve and relationships between lnθ, $-\partial(\ln\theta)/\partial\varepsilon$ and ε for the Al_2O_3-Cu/35Cr3TiB_2 composites deformed at 850 °C and 0.01 s^{-1} strain rate: (a) True stress-true strain curve, (b) lnθ-ε curve,

(c) -∂(ln θ)/∂ε-ε curve.

In the same way, the ∂(lnθ)/∂ε-ε curves of the two composites under different deformation conditions were obtained in Fig. 6, and the critical DRX strain values of the two composites show negative correlation with the deformation temperature and positive correlation with the strain rate. The addition of Y_2O_3 increases the composites' DRX critical strain values, implying that Y_2O_3 inhibited the DRX occurrence in the composites.

(a) 0.1 s^{-1}, (b) 0.01 s^{-1}, (c) 850 °C, (d) 950 °C.

By constructing a critical DRX model, the effects of different factors on the critical DRX strain can be more intuitively reflected from a mathematical point of view. The Sellars [35] model is a commonly used critical DRX model:

$$\varepsilon c = k\varepsilon p \tag{14}$$

$$\varepsilon c = aZb \tag{15}$$

$$ln\ \varepsilon c = ln\ a + b\ln Z \tag{16}$$

Here, ε_c is the critical strain, ε_p is the peak strain, the Z is expressed in Eq. (8), and the rest of the parameters are constants, the scatter plots of ε_p-ε_c and lnε_c-lnZ are plotted and linearly fitted, respectively in Fig. 7. The critical DRX strain model for the Al_2O_3-Cu/35Cr3TiB_2 composites can be derived as:

$$\varepsilon c = 1.23 \times 10 - 3Z0.134 \tag{17}$$

The critical DRX strain model for the 0.5Y_2O_3/Al_2O_3-Cu/35Cr3TiB_2 composites is:

$$\varepsilon c = 4.62 \times 10 - 3Z0.095 \tag{18}$$

It can be seen from the fitted equations for peak strain and critical DRX strain in Fig. 7, that DRX has occurred in both composites before the peak stress was reached, and the softening effect of DRX gradually dominated after reaching the peak stress. The critical DRX strain model can predict the strain corresponding to the occurrence of DRX in two composites under different deformation conditions, which is of great significance for analyzing the peak stresses, true stress-true strain curves and microstructure evolution of the materials.

3.4. Hot processing maps

The constitutive equation is an important way to predict hot deformation parameters, but it does not determine the advantages and disadvantages of material processing performance. Establishing the materials hot processing map through dynamic material model (DMM) can clarify the optimal hot deformation technology of materials and suggest suitable temperature and strain rate intervals for processing, to avoid materials loss and energy waste, which has a positive impact on the actual production of materials [36,37]. The total energy P required for hot deformation of a materials, including the energy G required for the materials to complete the deformation and the energy J required for the internal structure evolution of the materials, are related as in [38]:

$$P = G + J = \sigma\dot{\varepsilon} = \int_0^{\dot{\varepsilon}} \sigma d\dot{\varepsilon} + \int_0^{\sigma} \dot{\varepsilon} d\sigma \tag{19}$$

The sensitivity factor *m* determines the distribution of energy consumption:

$$m = \frac{dJ}{dG} = \left[\frac{\partial(ln\sigma)}{\partial(ln\dot{\varepsilon})}\right]_{\dot{\varepsilon},T} = \frac{d\ln\sigma}{d\ln\dot{\varepsilon}} \tag{20}$$

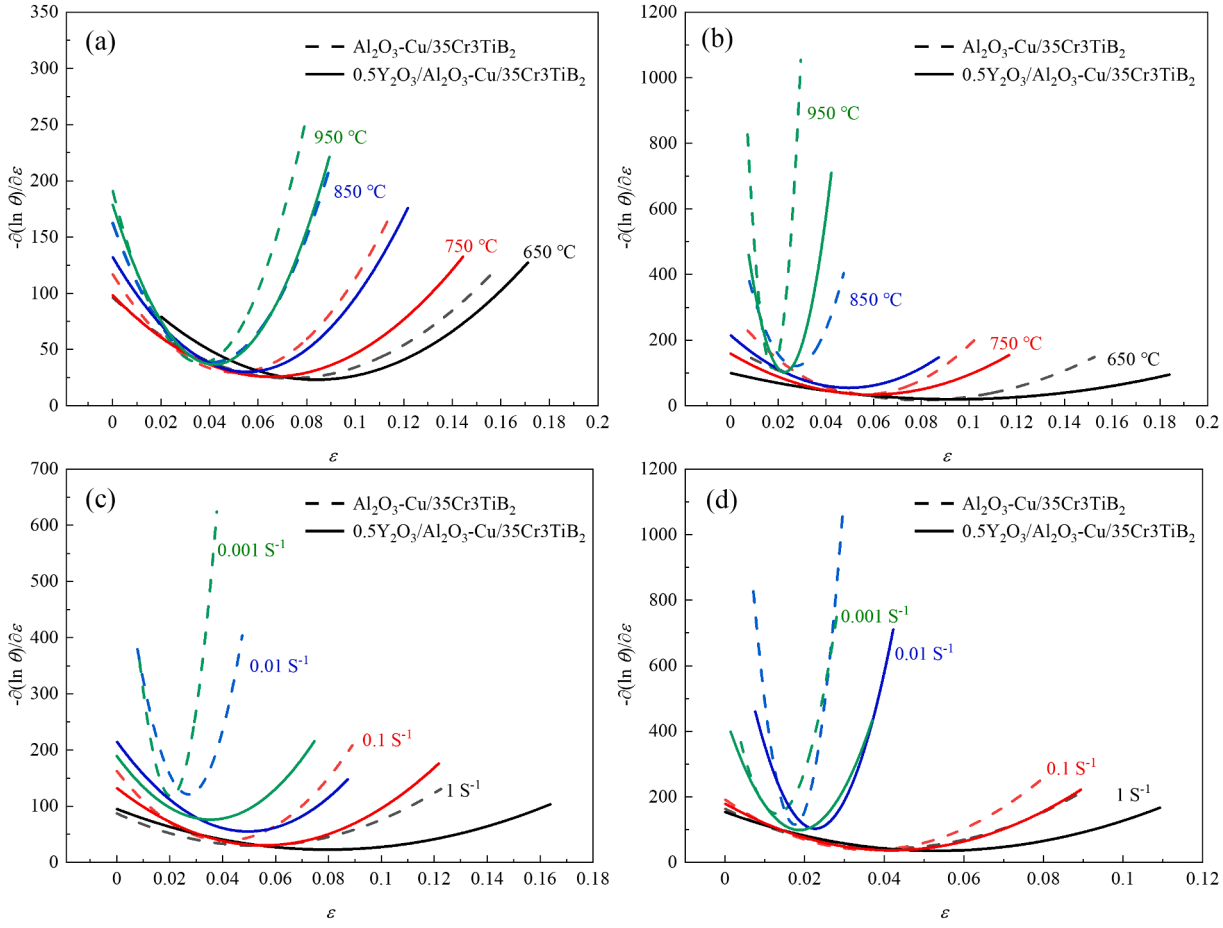

Fig. 6. Relationship between -∂(ln θ)/∂ε and ε for different deformation conditions of two composites:

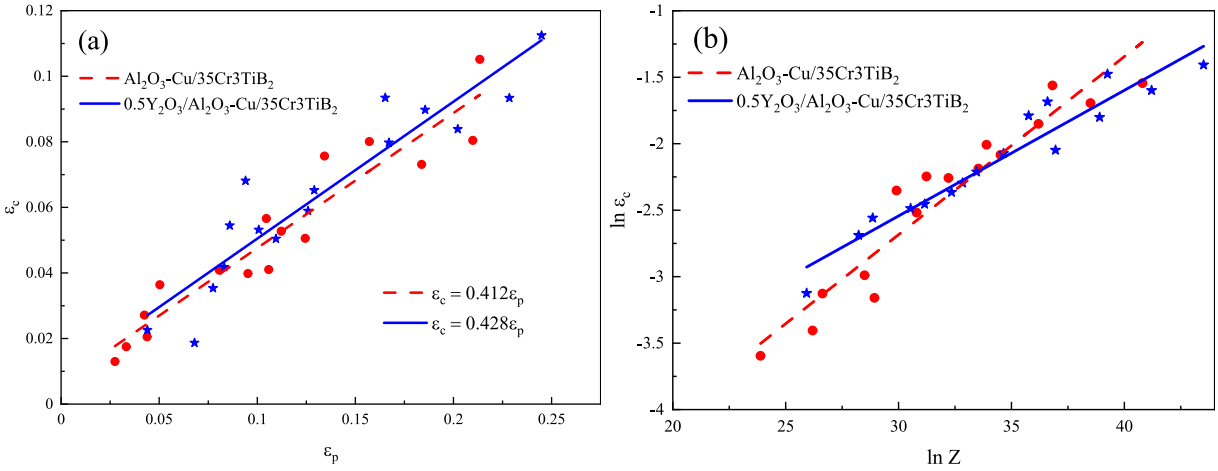

Fig. 7. Critical DRX strain linear fitting: (a) critical strain-peak strain, (b) ln ε_c-ln Z relation.

The power dissipation coefficient η is the ratio of J to the linear dissipation of energy during hot deformation:

$$\eta = \frac{J}{J_{max}} = \frac{2m}{m+1} \tag{21}$$

The instability criterion ξ is:

$$\xi(\dot{\varepsilon}) = \frac{\partial ln\left(\frac{m}{2m+1}\right)}{\partial(ln\dot{\varepsilon})} + m < 0 \tag{22}$$

When the criterion value ξ is below 0, it is the destabilization zone. Adding the destabilized region to the power dissipation map gives the hot processing map of the material in Fig. 8 for the two composites at 0.1, 0.3 and 0.5 strains, respectively. The contour lines in Fig. 8 depend on the power dissipation coefficient η, where higher values of the contour lines imply larger values of J, meaning that the energy acting inside the material to evolve the structure increases, making the material more susceptible to dynamic recovery and DRX. At the same time, because the total energy is constant, less energy is required to complete the deformation of the material, and the material will deform more readily, resulting in superior machinability. The shaded part in Fig. 8 is the destabilization zone, and machining within this interval may lead to failure, including cracks, holes, or even fragmentation of the material, and the destabilization zone should be avoided during machining.

It can be seen from Fig. 8 that the machining destabilization regions of both materials are mainly distributed in the low deformation temperature region or high strain rate region, which is consistent with the actual situation. The material is deformed at high strain rates and low temperatures, the dislocation density increases rapidly, and it is difficult for the material to undergo dynamic softening at low temperatures to

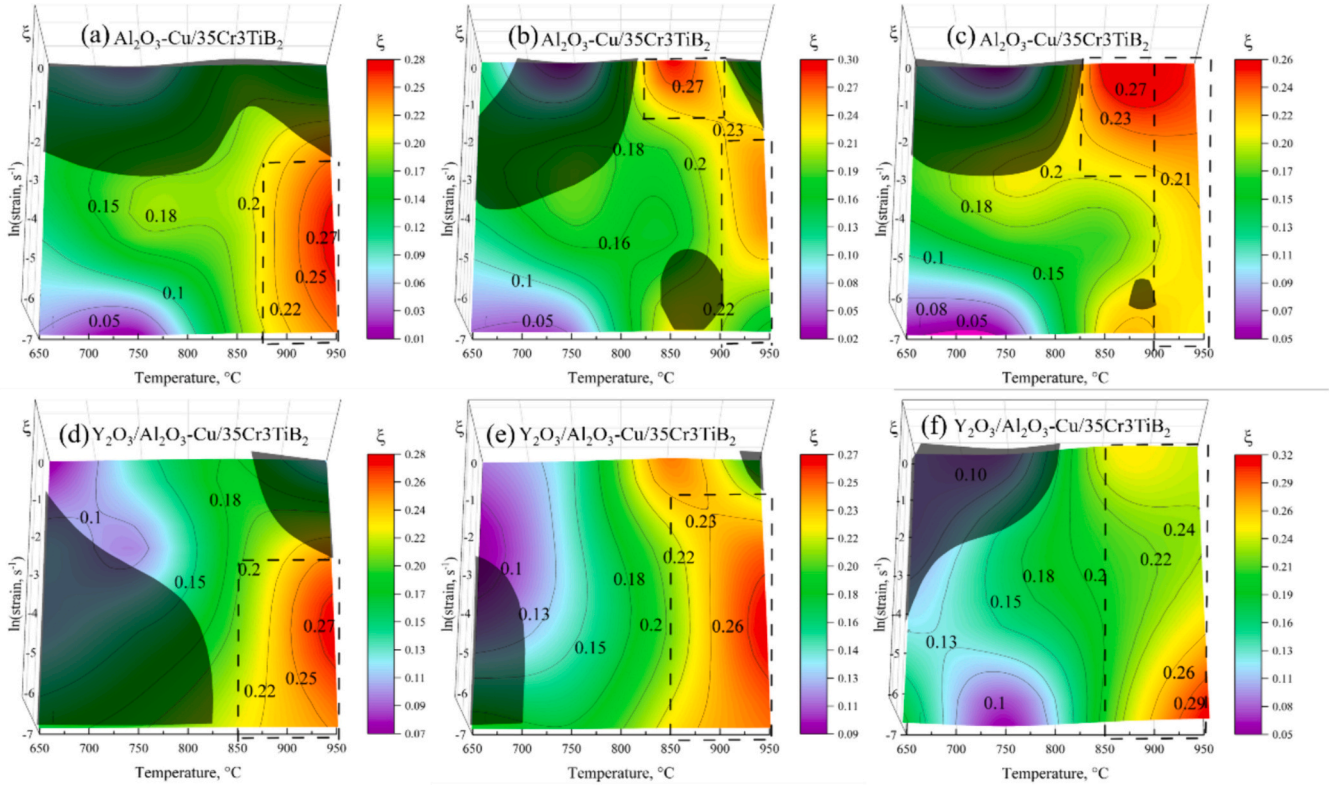

Fig. 8. Hot processing maps of the two composites at different strain: (a, d) ε = 0.1, (b, e) ε = 0.3, (c, f) ε = 0.5.

release the stresses, leading to stress concentrations and thus defects such as cracks in the material. In addition, the power dissipation diagrams of the two composites are almost identical in morphology, while the values of the contours are different. Similarly, the η values of both materials are at a higher level in the high temperature and low strain rate region, implying that the materials have better processing performance in this region.

The dashed boxed portion of Fig. 8 is the optimal machining region of the material at the corresponding strain. The optimal machining region of the Al_2O_3-Cu/35Cr3TiB_2 composites at 0.1, 0.3 and 0.5 strains is at 900–950 °C deformation temperature and 0.001–0.08 s^{-1} strain rate. Similarly, the optimal processing temperature of 0.5Y_2O_3/Al_2O_3-Cu/35Cr3TiB_2 composites is 850–950 °C at 0.001–0.07 s^{-1} strain rates. It is worth noting that the addition of Y_2O_3 reduces the destabilization region of the material during deformation under different conditions, while simultaneously augmenting the optimal processing region of the material, which has a positive effect on the hot processing properties of the material.

3.5. Microstructure evolution analysis

The microstructure of the two composites under different deformation conditions was characterized by the EBSD technique in Fig. 9 to investigate the effects of the Y_2O_3 addition along with different deformation temperatures and strain rates after the Y_2O_3 addition on the grain state and structure of the composites during the hot deformation process. The structure of the material after deformation shows obvious directionality, the Cu grains are elongated perpendicular to the axial direction, and the Cr and TiB_2 particles also move with the matrix so that the orientation tends to be the same in addition to the grain boundaries and phase interfaces where a relatively large number of DRX grains can be observed.

The size and distribution of grains are linked with the material's performance. There is a large difference in the size and distribution of grains between Cu, Cr and TiB_2, but the area of reinforcing phases contained in the scanning region of different samples is inconsistent. In order to better analyze the microstructure changes of the composites, the grain diameter of Cu matrix was counted in Fig. 9. It can be seen comparing Fig. 9(a, c) that the average grain size of the composites decreased by 0.9 μm with the Y_2O_3 addition under the same deformation conditions. On the one hand, the Y_2O_3 addition refines the grains in the sintered samples and reduces the average grain size of the composites. On the other hand, comparing the grain diameter distributions in Fig. 14(a_1) and Fig. 14(c_1) shows that the proportion of grains with sizes smaller than 2 μm is higher in the Al_2O_3-Cu/35Cr3TiB_2 composites. This suggests that the Y_2O_3 addition inhibits the occurrence of DRX, and the reduction of the fine grains generated by the matrix makes the 0.5Y_2O_3/Al_2O_3-Cu/35Cr3TiB_2 composites with elevated average grain size. Therefore, DRX does not occur sufficiently when deformed at 850 °C and 0.01 s^{-1}, and the refining effect of Y_2O_3 on the composites' grains dominates.

It can be seen comparing Fig. 9(b, c) that the degree and number of elongated grains increase with strain rate. The average grain size of the composites also has a tendency to increase with the strain rate. This is because at the same deformation temperature, the higher the strain rate, the shorter the time required for the material to reach the specified strain, the less sufficient DRX occurs within the material, and the generation of fine recrystallized grains decreases. It is worth noting that the higher deformation temperature promotes the motion of atoms and grain boundaries within the material, making DRX and grain growth of the 0.5Y_2O_3/Al_2O_3-Cu/35Cr3TiB_2 composites more likely to occur. It can be seen comparing Fig. 9(c_2, d_2) that the average grain size of the composites increases from 2.64 μm to 3.54 μm with deformation temperature. And the proportion of grains with size <3 μm decreased from 69% to 51%, and the proportion of grains with different size ranges all showed a decreasing trend, while the proportion of grains with size >4.5 μm increased from 11% to 31%, and the proportion of grains with different size ranges all showed an increasing trend. This indicates the growth phenomenon of DRX grains with smaller sizes, and the growth feature of DRX grains can be clearly observed by comparing Fig. 9(c, d). This is because the increase in temperature leads to a decrease in the bond energy between atoms, and the bonds are more easily broken. And the increase in temperature is conducive to the movement and diffusion of atoms inside the composite, the slip and climb of dislocations and the migration of grain boundaries are easier, and the essence of grain growth is the migration process of grain boundaries, grain growth will make the content of grain boundaries lower, thus reducing the interfacial energy. Therefore, as long as there are temperature and time conditions to meet the atomic diffusion, grain growth is spontaneous, and the higher the temperature, the more obvious the trend and speed of grain growth.

During hot deformation of the material, the grains will be compressed and deformed or even crushed, producing a large number of subcrystals and low-angle grain boundaries (LAGBs). When a material occurs DRX is usually nucleated with subcrystals as the core, and LAGBs gradually transform into large angular grain boundaries (HAGBs). Fig. 10 shows the distribution of grain boundaries and the statistics of grain boundary orientation angles of the two composites under different deformation conditions, where the orange lines represent LAGBs and the black lines represent HAGBs. The addition of Y_2O_3 inhibited the DRX and grain boundary motion of the composites, which made it difficult to transform the LAGBs into HAGBs, thus reducing the HAGBs content of the composites from 77.8% to 71.4%. The increase in strain rate also reduces the content of HAGBs. On the one hand, the material does not have enough time to undergo DRX, and on the other hand, higher strain rate results in a more severe deformation of the grains within the material, and a large number of grains are crushed to become equiaxed grains. As seen in Fig. 10(b_2), the content of grain boundaries with orientation angles lower than 5° increases abruptly, which also means that more grains are crushed. In agreement with the above analysis, the increase in temperature makes DRX and grain growth of the composites more likely to occur, and the migration of grain boundaries is more likely to occur, therefore the HAGBs content of the composites increases from 71.4% to 86.3%.

The kernel-averaged misorientation (KAM) can be used to characterize the stress distribution state of the composites during the deformation process, which is of great significance for microstructure analysis. While the density of geometrically necessary dislocations (GND) is directly proportional to the KAM value, the larger KAM value implies the higher density of GND in the region. It can be seen from Fig. 11 that the KAM value of the copper matrix is relatively larger and more widely distributed, indicating that the copper matrix has experienced a higher strain. Meanwhile the value of GND can be calculated from KAM as in [39]:

$$\rho\mathrm{GND} = 2\theta/\mu b \tag{23}$$

Here, θ is the average orientation (rad), μ is the electron microscope scanning step (μm), and b is the Burgers vector of copper (0.255 nm), the ρ^{GND} of the two composites under different deformation conditions can be obtained by calculation. It is worth noting that the hard phase hinders the movement of dislocations, so the GND density of 0.5Y_2O_3/Al_2O_3-Cu/35Cr3TiB_2 composites is higher under the same deformation conditions. It can be observed comparing Fig. 11(b, c) that an increase in strain rate causes a large increase in dislocation density, which is consistent with the distribution of LAGBs. On the contrary, when the deformation temperature increases, the GND density of the composites decreases from 3.05 × 10^{14} m^{-2} to 2.64 × 10^{14} m^{-2} as shown in Fig. 11(c, d), which demonstrates that dislocations are the driving force of DRX, which are consumed by both DRX occurrences and grain growth processes.

Fig. 12 shows the distribution of the deformed structures of the two composites under different deformation conditions, where the blue

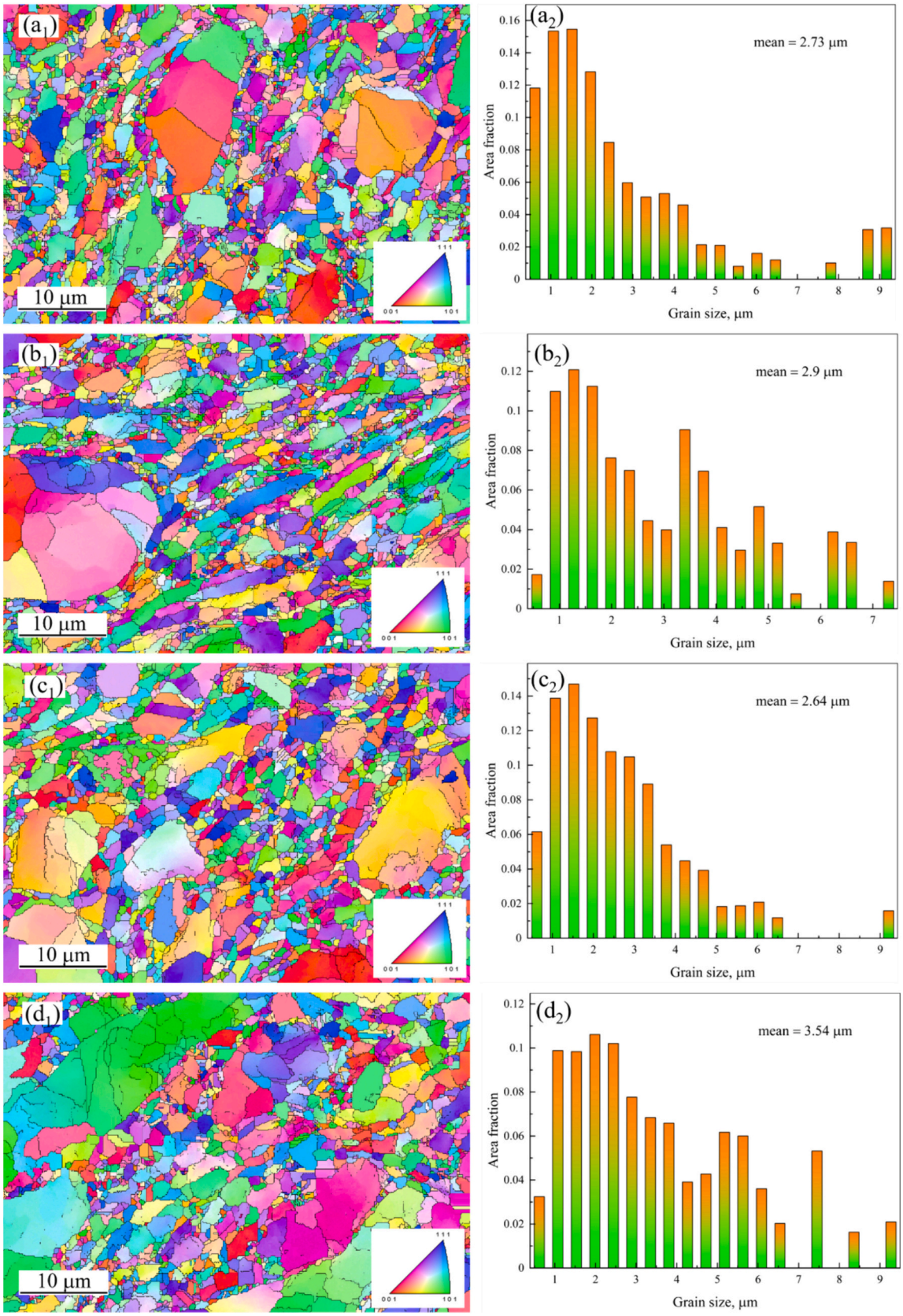

Fig. 9. EBSD images and grain size statistics of two composites after hot deformation: (a_1, a_2) Al_2O_3-Cu/35Cr3TiB_2 composites deformed at 850 °C and 0.01 s^{-1}, (b_1, b_2) 0.5Y_2O_3/Al_2O_3-Cu/35Cr3TiB_2 composites deformed at 850 °C and 0.1 s^{-1}, (c_1, c_2) 0.5Y_2O_3/Al_2O_3-Cu/35Cr3TiB_2 composites deformed at 850 °C and 0.01 s^{-1}, (d_1, d_2) 0.5Y_2O_3/Al_2O_3-Cu/35Cr3TiB_2 composites deformed at 950 °C and 0.01 s^{-1}.

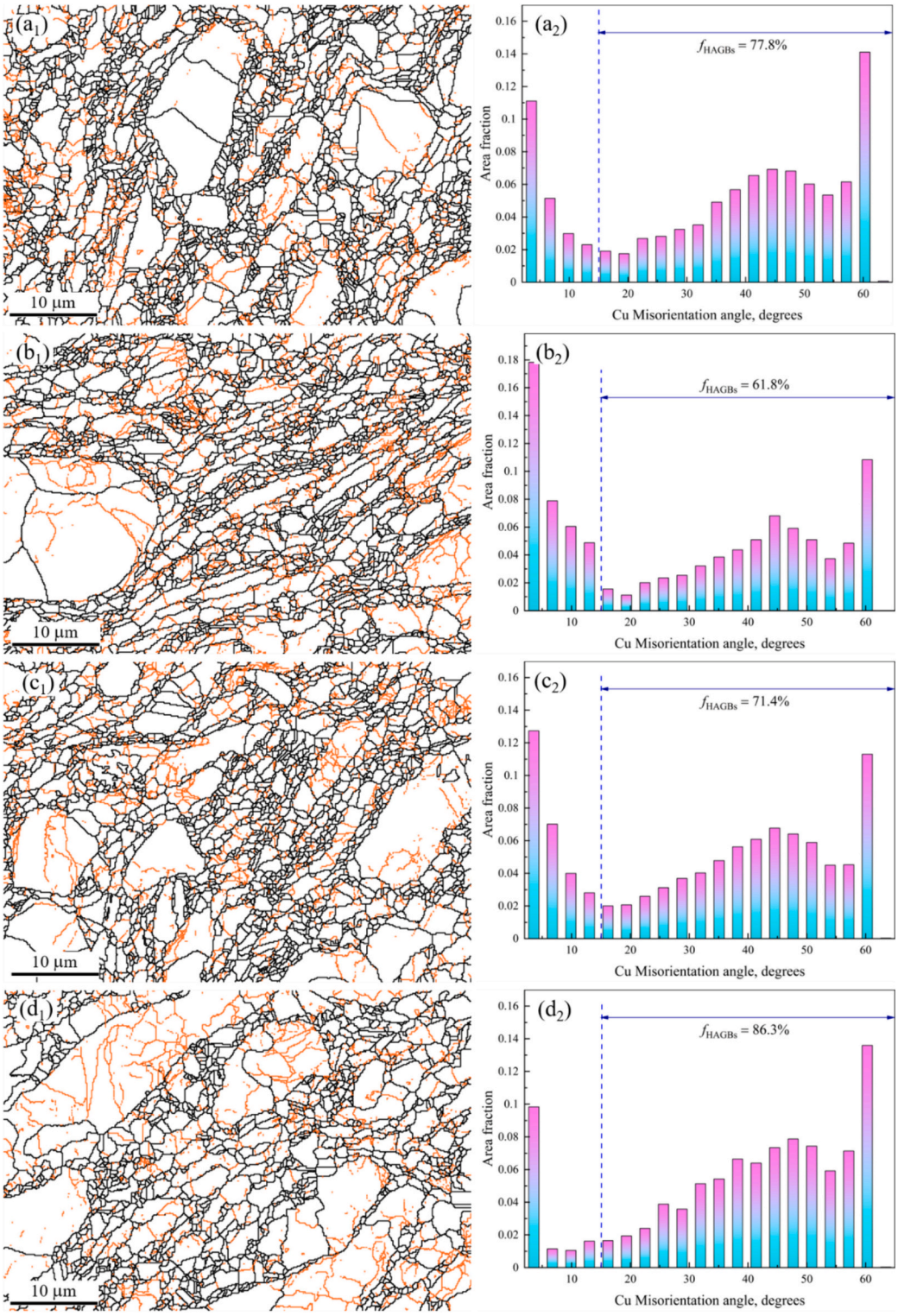

Fig. 10. Grain boundary map and orientation angle statistics of the two composites after hot deformation: (a_1, a_2) Al_2O_3-Cu/35Cr3TiB_2 composites deformed at 850 °C and 0.01 s^{-1}, (b_1, b_2) 0.5Y_2O_3/Al_2O_3-Cu/35Cr3TiB_2 composites deformed at 850 °C and 0.1 s^{-1}, (c_1, c_2) 0.5Y_2O_3/Al_2O_3-Cu/35Cr3TiB_2 composites deformed at 850 °C and 0.01 s^{-1}, (d_1, d_2) 0.5Y_2O_3/Al_2O_3-Cu/35Cr3TiB_2 composites deformed at 950 °C and 0.01 s^{-1}.

region is the recrystallized structure, the yellow region is the subcrystalline grain, and the red region is the deformed structure. It is worth noting that DRX grains are confirmed by Grain Orientation Spread (GOS). Where a GOS value of <1 is considered to be a DRX grain, a GOS value of 1 to 5 is considered to be a subcrystalline grain, and a GOS value of >5 is considered to be a deformed grain. The addition of Y_2O_3 reduces the percentage of recrystallized structure from 25.3% to 19.4%, which has a more obvious inhibiting effect on the DRX of the composites. This is due to the higher high-temperature stability of Y_2O_3, which hinders the movement of grain boundaries during sintering and cooling down with the furnace, thus refining the grains of the composites. The smaller the grain size, the more uniform the distribution of stresses and the

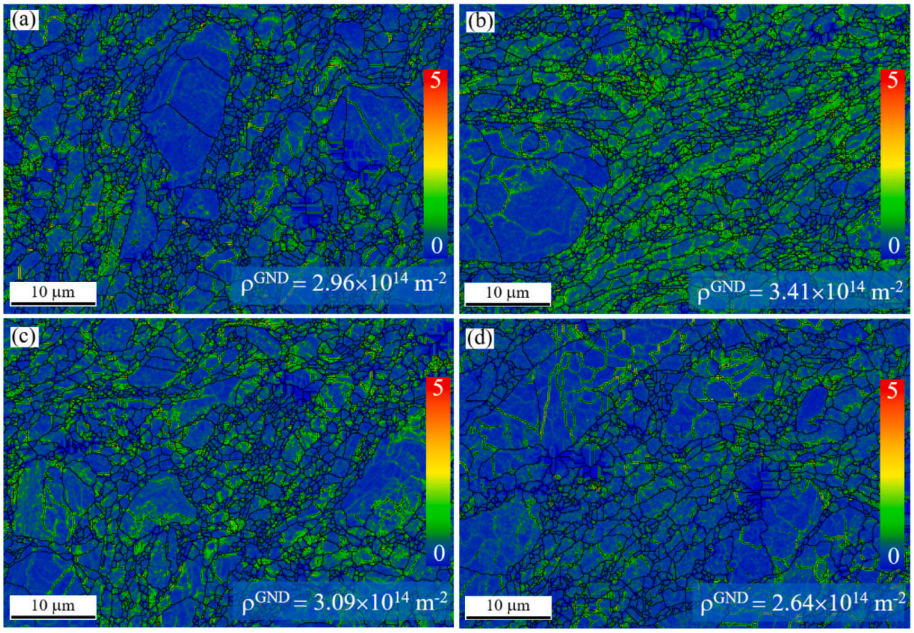

Fig. 11. KAM maps of the two composites: (a) Al_2O_3-Cu/35Cr3TiB_2 composites deformed at 850 °C and 0.01 s^{-1}, (b) 0.5Y_2O_3/Al_2O_3-Cu/35Cr3TiB_2 composites deformed at 850 °C and 0.1 s^{-1}, (c) 0.5Y_2O_3/Al_2O_3-Cu/35Cr3TiB_2 composites deformed at 850 °C and 0.01 s^{-1}, (d) 0.5Y_2O_3/Al_2O_3-Cu/35Cr3TiB_2 composites deformed at 950 °C and 0.01 s^{-1}.

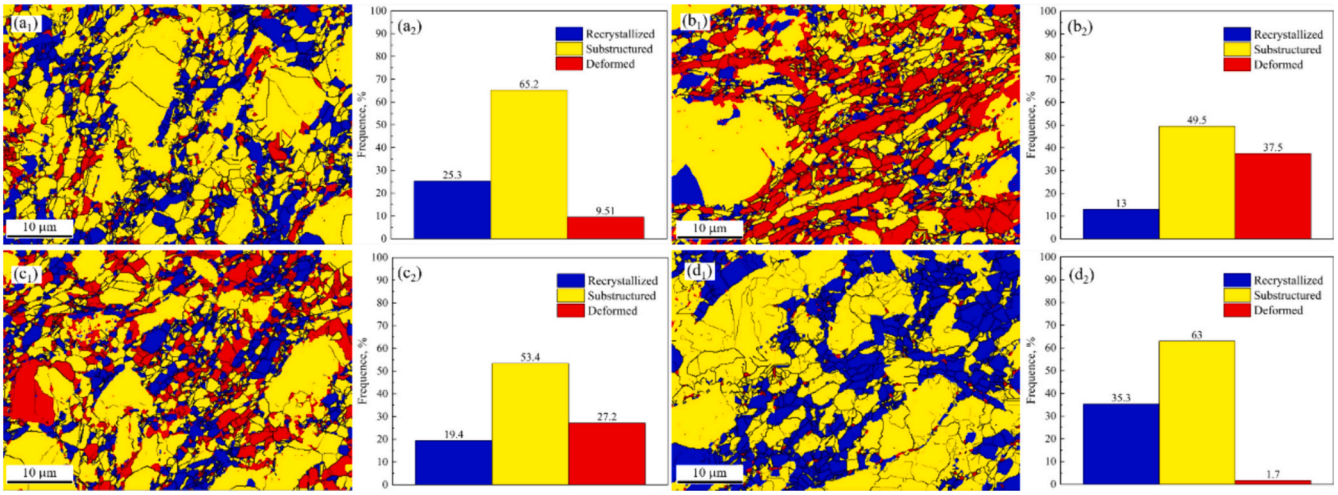

Fig. 12. Matrix structure characteristics and distribution of the two composites after hot deformation: (a_1, a_2) Al_2O_3-Cu/35Cr3TiB_2 deformed at 850 °C and 0.01 s^{-1}, (b_1, b_2) 0.5Y_2O_3/Al_2O_3-Cu/35Cr3TiB_2 deformed at 850 °C and 0.1 s^{-1}, (c_1, c_2) 0.5Y_2O_3/Al_2O_3-Cu/35Cr3TiB_2 deformed at 850 °C and 0.01 s^{-1}, (d_1, d_2) 0.5Y_2O_3/Al_2O_3-Cu/35Cr3TiB_2 deformed at 950 °C and 0.01 s^{-1}.

fewer the nucleation points to satisfy the driving force of DRX during the hot deformation of the material. At the same time, Y_2O_3 further hinders the movement of grain boundaries, making it more difficult for the material to undergo DRX.

The recrystallized structure of 0.5Y_2O_3/Al_2O_3-Cu/35Cr3TiB_2 composites decreases to 13% when deformed at 850 °C and 0.1 s^{-1} strain rate, where the content of deformed structure is the highest, reaching 37.5%. The higher dislocation density within the deformation structure has a positive effect on the mechanical properties of the composites, but the higher content of the deformation structure is prone to the formation of stress concentration zones that lead to failure phenomena such as cracking of the composites. The optimal processing region of the material does not contain a 0.1 s^{-1} strain rate, which is also a good proof of this point. When the deformation temperature is increased from 850 °C to 950 °C, the recrystallized structure inside the composites increases from 19.4% to 35.3%. The percentage of subcrystalline structure also increases. Subcrystalline grain is the process of polygonization of dislocations inside the deformed grains after deformation of the material, and subcrystalline grain boundaries appear inside the original deformed grains, which corresponds to the stage of slowly increasing stress in the true stress-strain curve. It can be concluded that the promotion of DRX of composites by increasing temperature is more obvious compared to the decrease of strain rate.

3.6. Microstructure analysis

The hot deformation experiments are used to study the high-temperature deformation behavior, strengthening mechanism and microstructure evolution of the materials. The microstructure of the composites after deformation was characterized by transmission

electron microscopy (TEM). Fig. 13 shows the microstructure of Al_2O_3-Cu/35Cr3TiB_2 composites after hot deformation. The uniformly distributed γ-Al_2O_3 in the Cu matrix and its pinned fine dislocations can be seen in Fig. 13(a). Fig. 13(b) is the high-resolution TEM (HRTEM) image of Fig. 13(a), and the fast Fourier transform (FFT) images of the three regions A_1, A_2 and A_3 in Fig. 13(b) were analyzed, which correspond to the TiB_2, Cu and γ-Al_2O_3 phases, respectively. Through the corresponding inverse FFT (IFFT) and gray-scale spectrograms, the crystal plane spacing was obtained to be 0.261 nm, 0.214 nm, and 0.456 nm for $(100)_{TiB2}$, $(111)_{Cu}$, and $(111)_{Al2O3}$. It can also be seen that the γ-Al_2O_3 generated by internal oxidation is bonded with the copper matrix.

In the early stage of material deformation, stresses are first concentrated at grain boundaries and defects, accompanied by the generation and movement of dislocations. The presence of hard phases in the matrix hinders the movement of dislocations and increases the internal stress level of the material, leading to a large amount of cross-slip migration of the dislocations, which further increases the dislocation density. In Fig. 13(a) dislocations are entangled around the hard TiB_2 phase. In addition, these cross-slips react with the dislocations to form prismatic dislocation rings [40]. As the material continues to deform, these dislocation rings act as the centers of the dislocation entanglement to form a cellular structure in Fig. 13(d). As the material deforms at high temperatures, the dynamic recovery consumes dislocations, which narrows the walls of these dislocation cells, and finally deformed subcrystals are gradually formed in Fig. 13(e), and clear deformed subcrystal boundaries can be seen in Fig. 13(f).

In order to investigate the effects of Y_2O_3 on the microstructure of the composites after hot deformation, the TEM images of 0.5Y_2O_3/Al_2O_3-Cu/35Cr3TiB_2 composites under the same deformation conditions were analyzed. It is noteworthy that a large number of dislocation entanglements and deformed structures were found inside the material as well. The hindering effect of Y_2O_3 particles on dislocations can be clearly observed in Fig. 14(a). Fig. 14(c) demonstrates the interfacial structure between the Cr particles and the Cu matrix, where smaller hard particles can be seen inside the material concentrated at the phase interfaces of Cu—Cr, Cu-TiB_2, and TiB_2 particles distributed at grain boundaries in Fig. 14(e). This is because the hard phase will hinder the movement of the interface, so in the formation and growth of grain boundaries, the hard particles gradually crowd out to the interface positions, where the interface energy is usually higher. The enhanced phase at the interface can reduce the interfacial energy, so that the material interfacial system is more stable. In addition, the reinforcing phase can act as an interchange and absorption source of dislocations when it is at the grain boundaries, which can promote the self-adjustment of the grain boundaries to a certain extent and improve the structure and properties of the crystals. However, with the increase of deformation and dislocation density, the stress between the reinforcing phase and the interface increases, which will lead to the appearance of microcracks and other defects affecting the macroscopic properties and use of the material. In addition, the sizes of Y_2O_3 particles and γ-Al_2O_3 particles were quantitatively analyzed as shown in Fig. 14(f) and Fig. 14(g), and it is found that most of the Y_2O_3 particles are smaller than 50 nm, and most of the γ-Al_2O_3 particles are smaller than 5 nm, which provide good reinforcement to the matrix.

Fig. 14(h) shows the HRTEM image at the phase interface of Fig. 14(c), which proves the existence of Y_2O_3 at the phase interface by the calibration of the regional diffraction spots and the spacing of the

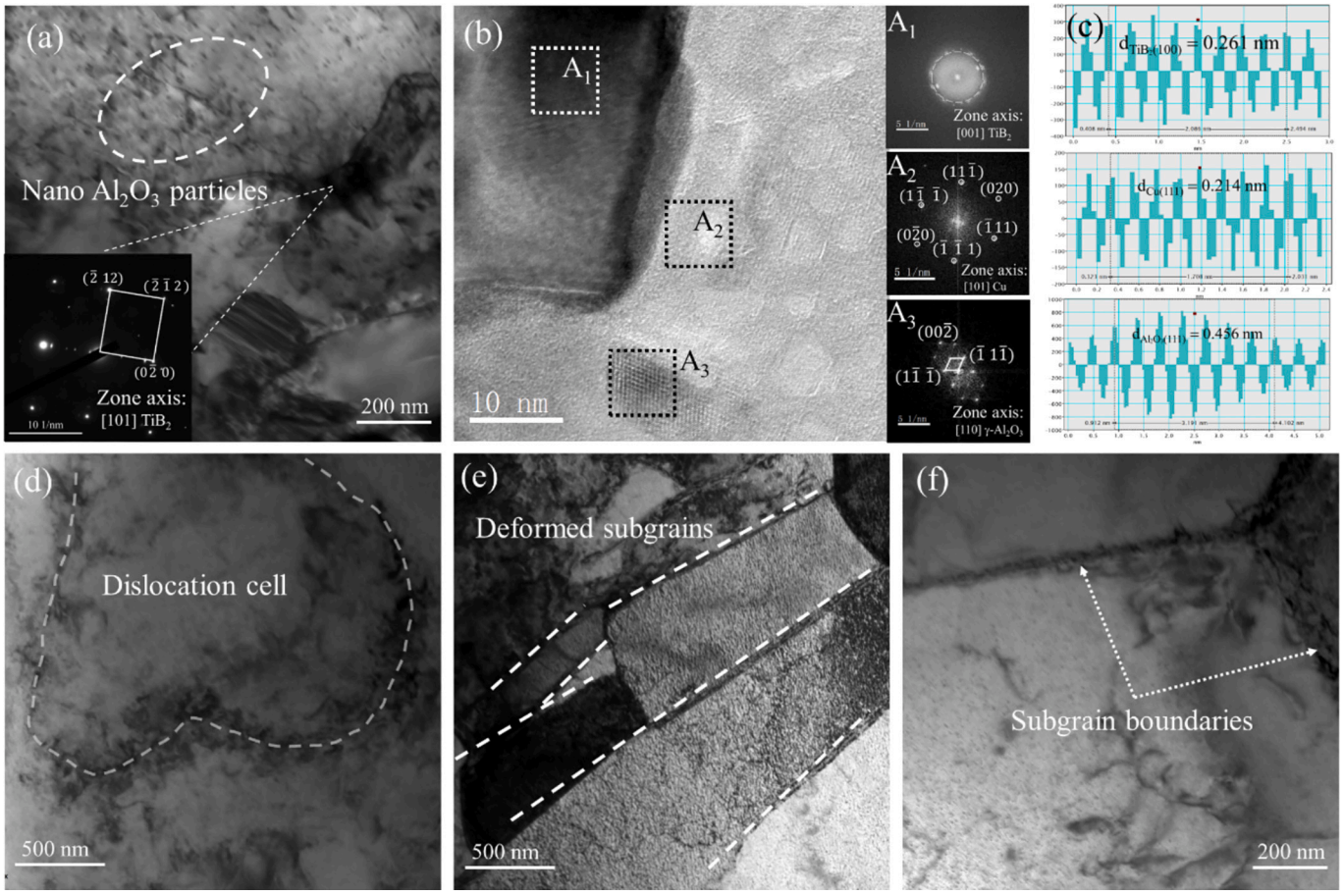

Fig. 13. TEM images of the Al_2O_3-Cu/35Cr3TiB_2 composites deformed at 850 °C and 0.01 s^{-1}: (a, d, e, f) TEM images of the composites, (b) HRTEM image of (a), (c) gray-scale spectrogram of (b).

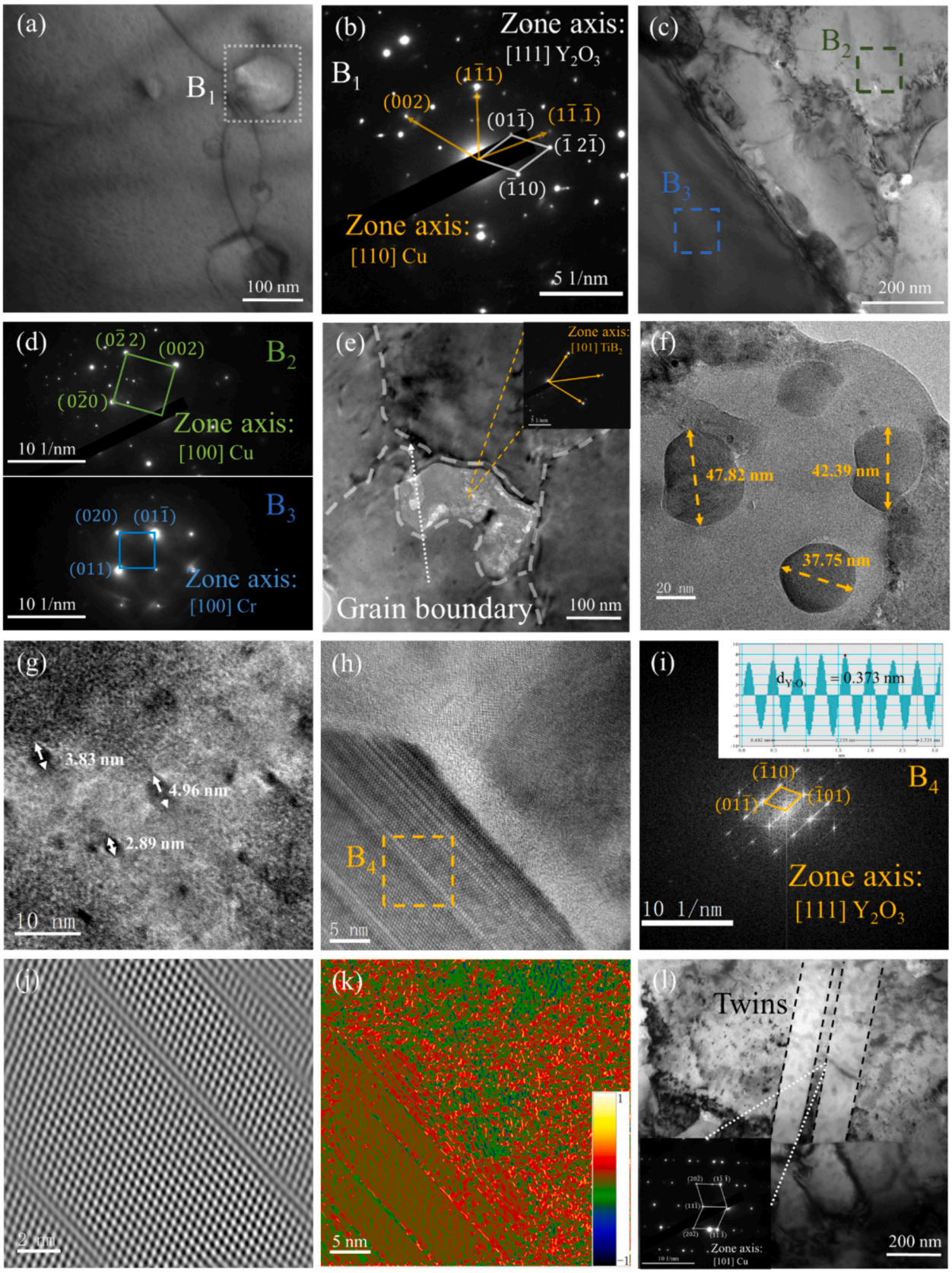

Fig. 14. TEM images of $0.5Y_2O_3/Al_2O_3$-Cu/35Cr3TiB_2 composites after hot deformation at 850 °C, 0.01 s^{-1}: (a, c, e, f, g, h, l) TEM images of composites, (b) FFT images of regions B_1 in (c), (d) FFT images of regions B_2, B_3 in (c), (h) HRTEM image of (c), (i) FFT image of the B_4 region in (h), (j) corresponding IFFT image in (h), (k) GPA image of (h).

crystalline faces. More defects are observed in the interior of the Y_2O_3 particles. It can be seen from Fig. 14(i) that the spots at the [$\bar{1}$01] band axis are elongated into a single line under the [110] band-axis incidence condition. This indicates that there is a misalignment of atomic faces in the region in Fig. 14(h), and it can be judged that the face defects here are stacking faults. Stacking faults can reinforce the copper substrate by changing the direction dislocation slip, increasing the stress required for dislocations to cross-slip, forming immovable dislocation locks, and impeding dislocation movement. On the other hand, the absorbing effect of the stacking faults on the dislocations avoids the plugging and stress concentration of the dislocations to a large extent, which can effectively improve the ability of plastic deformation of the material. Geometric phase analysis (GPA) can more accurately analyze the small strains in the HRTEM images, and Fig. 14(k) is the GPA corresponding to Fig. 14 (h), where the strains of Y_2O_3 are more homogeneous, while the Cu matrix exhibits non-uniform strains. In addition, more twins are found inside the Cu matrix, which can hinder dislocation motion and grain boundary migration, and play an important role in the strengthening of the material.

4. Conclusions

(1) The Cr, TiB_2 and the γ-Al_2O_3 particles generated by internal oxidation were uniformly distributed in the Cu matrix, which were well combined with the Cu matrix. The Y_2O_3 was distributed at grain boundaries and phase interfaces, hindering the movement of grain boundaries and dislocations.
(2) The true stress-true strain curves of the two composites showed DRX characteristics, and the addition of Y_2O_3 increases the activation energy by 10.4% and inhibits the DRX of the composites. Moreover, compared with the decrease of strain rate, the increase of temperature promotes the DRX of the composites more significantly.
(3) Hot processing maps were established to determine the optimal processing range of the two composites. The addition of Y_2O_3 reduced the processing destabilization region of the composites and improved the hot processing technological performance of the composites.
(4) A significant number of twins and stacking faults were observed within the $0.5Y_2O_3/Al_2O_3$-Cu/35Cr3TiB_2 composites, which can improve the strength and plasticity of the material and act as a synergistic reinforcement of the matrix.

CRediT authorship contribution statement

Zipeng Ma: Writing – original draft, Validation, Investigation, Formal analysis. **Meng Zhou:** Supervision, Funding acquisition. **Heng Li:** Investigation. **Ke Jing:** Supervision. **Jiacan Zhang:** Investigation. **Baohong Tian:** Methodology. **Yi Zhang:** Resources, Funding acquisition. **Xu Li:** Resources. **Haoyan Hu:** Investigation. **Alex A. Volinsky:** Resources.

Declaration of competing interest

The authors declare that they have no known competing financial interests or personal relationships that could have appeared to influence the work reported in this paper.

Data availability

The data will be made available from the corresponding author upon reasonable request.

Acknowledgments

This work was supported by the National Natural Science Foundation of China (52071134, 52374367), the Program for Innovative Research Team at the University of the Henan Province (22IRTSTHN001), Leading Talents of Science and Technology in the Central Plain of China (244200510029), Youth Talent Lifting Project of Heluo (2023HLTJ12), the Joint Foundation for Science and Technology Research and Development Plan of Henan Province (232103810030, 232103810031), Key Research and Development Program of Henan Province (231111232000, 231111231300).

References

[1] H.B. Xie, W.M. Guan, H. Lv, H.Y. Yang, M.Y. Gao, Y.T. Fang, J.B. Liu, H.T. Wang, W-cu/cu composite electrodes fabricated via laser surface alloying, Mater. Charact. 185 (2022) 8, https://doi.org/10.1016/j.matchar.2021.111715.
[2] T. Varol, A. Canakci, Microstructure, electrical conductivity and hardness of multilayer graphene/copper nanocomposites synthesized by flake powder metallurgy, Met. Mater. Int. 21 (2015) 704–712, https://doi.org/10.1007/s12540-015-5058-6.
[3] J.Y. Zhang, J.T. Zhao, X.G. Li, Y.Q. Wang, K. Wu, G. Liu, J. Sun, Alloying effects on the microstructure and mechanical properties of nanocrystalline cu-based alloyed thin films: miscible cu-Ti vs immiscible cu-Mo, Acta Mater. 143 (2018) 55–66, https://doi.org/10.1016/j.actamat.2017.09.039.
[4] X.H. Zhang, Y. Zhang, B.H. Tian, Y.L. Jia, M. Fu, Y. Liu, K.X. Song, A.A. Volinsky, X. Yang, H. Sun, Graphene oxide effects on the properties of Al_2O_3-cu/35W5Cr composite, J. Mater. Sci. Technol. 37 (2020) 185–199, https://doi.org/10.1016/j.jmst.2019.08.014.
[5] X.H. Zheng, M. Zhou, Y. Zhang, J.L. Huang, Y.Z. Li, H.J. Zhu, S.L. Tang, D. Li, S. L. Liang, B.H. Tian, Y. Liu, X. Li, Y.L. Jia, A.A. Volinsky, Microstructure and electrical contact behavior of Al_2O_3-cu/30W3SiC(0.5Y_2O_3) composites, J. Mater. Res. Technol. 22 (2023) 2158–2173, https://doi.org/10.1016/j.jmrt.2022.12.071.
[6] S. Batool, M. Idrees, S.T. Han, V.A.L. Roy, Y. Zhou, Electrical contacts with 2D materials: current developments and future prospects, Small 19 (2023) 20, https://doi.org/10.1002/smll.202206550.
[7] W.J. Li, Z.Y. Chen, H. Jiang, X.H. Sui, C.F. Zhao, L. Zhen, W.Z. Shao, Effects of interfacial wettability on arc erosion behavior of Zn_2SnO_4/cu electrical contacts, J. Mater. Sci. Technol. 109 (2022) 64–75, https://doi.org/10.1016/j.jmst.2021.08.045.
[8] X.H. Zhang, Y. Zhang, B.H. Tian, J.C. An, Z. Zhao, A.A. Volinsky, Y. Liu, K.X. Song, Arc erosion behavior of the Al_2O_3-cu/(W, Cr) electrical contacts, Compos. Pt. B-Eng. 160 (2019) 110–118, https://doi.org/10.1016/j.compositesb.2018.10.040.
[9] T. Varol, A. Canakci, The effect of type and ratio of reinforcement on the synthesis and characterization cu-based nanocomposites by flake powder metallurgy, J. Alloys Compd. 649 (2015) 1066–1074, https://doi.org/10.1016/j.jallcom.2015.07.008.
[10] T. Varol, A. Canakci, An investigation on wear behavior of cu-graphite nanocomposites prepared by flake powder metallurgy, Ind. Lubr. Tribol. 69 (2017) 8–14, https://doi.org/10.1108/ILT-11-2015-0187.
[11] H.L. Shi, W.M. Gan, C. Esling, X.J. Wang, Y.D. Zhang, E. Maawad, A. Stark, X.H. Li, L.D. Wang, Elastic strain induced abnormal grain growth in graphene nanosheets (GNSs) reinforced copper (cu) matrix composites, Acta Mater. 200 (2020) 338–350, https://doi.org/10.1016/j.actamat.2020.09.017.
[12] S.L. Liang, M. Zhou, Y. Zhang, S. Liu, X. Li, B.H. Tian, Y.F. Geng, Y.J. Ban, Y.L. Jia, Y. Liu, A.A. Volinsky, Thermal deformation behavior of GO/CeO_2 in-situ reinforced Cu30Cr10W electrical contact material, J. Alloys Compd. 899 (2022) 12, https://doi.org/10.1016/j.jallcom.2021.163266.
[13] L. Varoto, J.J. Blandin, P. Lhuissier, S. Roure, A. Papillon, M. Chosson, G. Martin, 3D microstructure characterization of cu-25Cr solid state sintered alloy using X-ray computed tomography and machine learning assisted segmentation, Mater. Charact. 203 (2023) 12, https://doi.org/10.1016/j.matchar.2023.113107.
[14] C.L. Cramer, J.W. McMurray, M.J. Lance, R.A. Lowden, Reaction-bond composite synthesis of SiC-TiB_2 by spark plasma sintering/field-assisted sintering technology (SPS/FAST), J. Eur. Ceram. Soc. 40 (2020) 988–995, https://doi.org/10.1016/j.jeurceramsoc.2019.11.061.
[15] H. Wang, H. Zhang, X. Cheng, L. Liu, S. Chang, X. Mu, Y. Ge, Microstructure and mechanical properties of GNPs and in-situ TiB hybrid reinforced Ti-6Al-4V matrix composites with 3D network architecture, Mater. Sci. Eng. A-Struct. Mater. Prop. Microstruct. Process. 854 (2022) 12, https://doi.org/10.1016/j.msea.2022.143536.
[16] R.R. Eleti, T. Bhattacharjee, A. Shibata, N. Tsuji, Unique deformation behavior and microstructure evolution in high temperature processing of HfNbTaTiZr refractory high entropy alloy, Acta Mater. 171 (2019) 132–145, https://doi.org/10.1016/j.actamat.2019.04.018.
[17] H.A. Derazkola, E. Garcia, A. Murillo-Marrod, A.C. Fernandez, Review on modeling and simulation of dynamic recrystallization of martensitic stainless steels during bulk hot deformation, J. Mater. Res. Technol. 18 (2022) 2993–3025, https://doi.org/10.1016/j.jmrt.2022.03.179.
[18] N. Stanford, M.D. Callaghan, B. de Jong, The effect of rare earth elements on the behaviour of magnesium-based alloys: part 1-hot deformation behaviour, Mater.

Sci. Eng. A-Struct. Mater. Prop. Microstruct. Process. 565 (2013) 459–468, https://doi.org/10.1016/j.msea.2012.12.023.
[19] A. Chaudhuri, A.N. Behera, A. Sarkar, R. Kapoor, R.K. Ray, S. Suwas, Hot deformation behaviour of Mo-TZM and understanding the restoration processes involved, Acta Mater. 164 (2019) 153–164, https://doi.org/10.1016/j.actamat.2018.10.037.
[20] H.J. Zhu, M. Zhou, K. Jing, B.H. Tian, Y. Zhang, X. Li, Y.Z. Li, X.H. Zheng, H. Li, Z. P. Ma, Y. Liu, A.A. Volinsky, J. Zou, Hot deformation behavior of $0.5Y_2O_3/Al_2O_3$-cu/ 30Mo3SiC composites doped with reduced graphene oxide, J. Mater. Res. Technol. 26 (2023) 7444–7459, https://doi.org/10.1016/j.jmrt.2023.09.031.
[21] W.C. Zhuang, Z.Y. Huang, W.Q. Hu, Q. Yu, H.J. Wang, X. Li, Y.B. Wu, Y. Zhou, Study of microstructure and mechanical properties of quasi-continuous network structured (Ti_3AlC_2-Al_3Ti)/2024Al composites based on hot rolling, J. Alloys Compd. 968 (2023) 11, https://doi.org/10.1016/j.jallcom.2023.171936.
[22] L.H. Li, S. Liu, M. Zhou, Y. Zhang, S.L. Liang, J.L. Huang, B.H. Tian, Y.F. Geng, Y. J. Ban, Y. Liu, Y.L. Jia, X. Li, A.A. Volinsky, Microstructure evolution of graphene reinforced cu/CeO_2/Cr electrical contact materials under thermal deformation behavior, J. Mater. Res. Technol. 18 (2022) 1412–1423, https://doi.org/10.1016/j.jmrt.2022.03.038.
[23] X.W. Feng, D.P. Zhang, B. Feng, Y.F. Lin, J. Wang, K.H. Zheng, Microstructure and properties of cu-0.4 wt.% Al2O3 composites fabricated by hot extrusion and cold drawing, J. Mater. Eng. Perform. 31 (2022) 1241–1249, https://doi.org/10.1007/s11665-021-06247-5.
[24] Y.J. Ban, Y. Zhang, Y.L. Jia, B.H. Tian, A.A. Volinsky, X.H. Zhang, Q.F. Zhang, Y. F. Geng, Y. Liu, X. Li, Effects of Cr addition on the constitutive equation and precipitated phases of copper alloy during hot deformation, Mater. Des. 191 (2020) 11, https://doi.org/10.1016/j.matdes.2020.108613.
[25] P. Xiao, Y.M. Gao, F.X. Xu, S.S. Yang, Y.F. Li, B. Li, S.Y. Zhao, Hot deformation behavior of in-situ nanosized TiB_2 particulate reinforced AZ91 mg matrix composite, J. Alloys Compd. 798 (2019) 1–11, https://doi.org/10.1016/j.jallcom.2019.05.244.
[26] X.R. Chen, Z.M. Xu, D.F. Fu, H. Zhang, J. Teng, F.L. Jiang, Comparative hot workability characteristics of an Al-Si/SiCp Aluminium matrix composite hybrid reinforced with various TiB_2 additions, Met. Mater.-Int. 27 (2021) 1880–1891, https://doi.org/10.1007/s12540-019-00585-9.
[27] D.Y. Xu, M. Zhou, Y. Zhang, S.L. Tang, Z.Y. Zhang, Y. Liu, B.H. Tian, X. Li, Y.L. Jia, A.A. Volinsky, D. Li, Q.J. Liu, Microstructure and hot deformation behavior of the cu-Sn-Ni-Zn-Ti (-Y) alloy, Mater. Charact. 196 (2023) 13, https://doi.org/10.1016/j.matchar.2022.112559.
[28] H. Ahamed, V. Senthilkumar, Hot deformation behavior of mechanically alloyed Al6063/$0.75Al_2O_3$/$0.75Y_2O_3$ nano-composite-a study using constitutive modeling and processing map, Mater. Sci. Eng. A-Struct. Mater. Prop. Microstruct. Process. 539 (2012) 349–359, https://doi.org/10.1016/j.msea.2012.01.109.
[29] Z.P. Ma, M. Zhou, B.H. Tian, Y. Zhang, H. Li, X. Li, J. Zou, H.Y. Hu, K. Jing, Y. Liu, A.A. Volinsky, Nano-Y_2O_3 effects on the electrical contact properties of Al_2O_3-cu/35Cr3TiB_2 composites, Mater. Charact. 207 (2024) 14, https://doi.org/10.1016/j.matchar.2023.113474.
[30] Y.F. Geng, Y. Zhang, K.X. Song, Y.L. Jia, X. Li, H.R. Stock, H.L. Zhou, B.H. Tian, Y. Liu, A.A. Volinsky, X.H. Zhang, P. Liu, X.H. Chen, Effect of Ce addition on microstructure evolution and precipitation in cu-co-Si-Ti alloy during hot deformation, J. Alloys Compd. 842 (2020) 14, https://doi.org/10.1016/j.jallcom.2020.155666.
[31] C.M. Sellars, W.J. McTegart, On the mechanism of hot deformation, Acta Metall. 14 (1966) 1136–1138, https://doi.org/10.1016/0001-6160(66)90207-0.
[32] Z. Savaedi, R. Motallebi, H. Mirzadeh, A review of hot deformation behavior and constitutive models to predict flow stress of high-entropy alloys, J. Alloys Compd. 903 (2022) 21, https://doi.org/10.1016/j.jallcom.2022.163964.
[33] X.F. Tang, B.Y. Wang, N. Zhang, Y.M. Huo, J. Zhou, Modeling of microstructural evolution and flow behavior of superalloy IN718 using physically based internal state variables, Rare Metals 41 (2022) 2759–2766, https://doi.org/10.1007/s12598-015-0602-6.
[34] E.I. Poliak, J.J. Jonas, Initiation of dynamic recrystallization in constant strain rate hot deformation, ISIJ Int. 43 (2003) 684–691, https://doi.org/10.2355/isijinternational.43.684.
[35] C.M. Sellars, J.A. Whiteman, Recrystallization and grain growth in hot rolling, Metal Sci. 13 (1979) 187–194, https://doi.org/10.1179/msc.1979.13.3-4.187.
[36] L.L. Wang, R.B. Li, Y.G. Liao, M. Jin, Study on characterization of hot deformation of 403 steel, Mater. Sci. Eng. A-Struct. Mater. Prop. Microstruct. Process. 567 (2013) 84–88, https://doi.org/10.1016/j.msea.2012.12.063.
[37] W.H. Liao, C.W. Tsai, Y.C. Tzeng, W.R. Wang, C.S. Chen, J.W. Yeh, Exploring hot deformation behavior of equimolar CoCrFeNi high-entropy alloy through constitutive equations and microstructure characterization, Mater. Charact. 205 (2023) 9, https://doi.org/10.1016/j.matchar.2023.113234.
[38] J.L. Yang, G.F. Wang, X.Y. Jiao, Y. Li, Q. Liu, High-temperature deformation behavior of the extruded Ti-22Al-25Nb alloy fabricated by powder metallurgy, Mater. Charact. 137 (2018) 170–179, https://doi.org/10.1016/j.matchar.2018.01.019.
[39] Y.S. Wu, X.Z. Qin, C.S. Wang, L.Z. Zhou, Influence of phosphorus on hot deformation microstructure of a Ni-Fe-Cr based alloy, Mater. Sci. Eng. A-Struct. Mater. Prop. Microstruct. Process. 768 (2019) 11, https://doi.org/10.1016/j.msea.2019.138454.
[40] X.H. Zhang, Y. Zhang, B.H. Tian, Y.L. Jia, Y. Liu, K.X. Song, A.A. Volinsky, Thermal deformation behavior of the Al_2O_3-cu/(W, Cr) electrical contacts, Vacuum 164 (2019) 361–366, https://doi.org/10.1016/j.vacuum.2019.03.054.